Available online at www.sciencedirect.com
ScienceDirect
Journal of Solid State Chemistry 179 (2006) 3870–3876
JOURNAL OF SOLID STATE CHEMISTRY
www.elsevier.com/locate/jssc

Crystal structures and phase transitions of $SrZr(PO_4)_2$–$BaZr(PO_4)_2$ solid solutions

Koichiro Fukuda*, Tomoyuki Iwata, Akira Moriyama, Shinobu Hashimoto

Department of Environmental and Materials Engineering, Nagoya Institute of Technology, Nagoya 466-8555, Japan

Received 5 July 2006; received in revised form 17 August 2006; accepted 17 August 2006
Available online 25 August 2006

Abstract

A complete series of solid solutions was prepared in the $SrZr(PO_4)_2$–$BaZr(PO_4)_2$ system and examined by conventional X-ray powder diffraction (XRPD). The crystals of $Sr_xBa_{1-x}Zr(PO_4)_2$ with $x \leqslant 0.1$ were isomorphous with yavapaiite ($KFe(SO_4)_2$, space group $C2/m$). The solid solution with $0.2 \leqslant x \leqslant 0.7$ has been composed of a new phase, showing a superstructure along the a-axis (c-axis of the yavapaiite substructure). The crystals with $0.8 \leqslant x \leqslant 0.9$ were composed of both the new phase and the triclinic phase, the latter being isostructural with $SrZr(PO_4)_2$ ($x = 1$). The crystal structure of the new phase has been determined using direct methods, and it has been further refined by the Rietveld method. The crystal of $Sr_{0.7}Ba_{0.3}Zr(PO_4)_2$ ($x = 0.7$) is monoclinic (space group $P2/c$, $Z = 4$ and D_x/$Mg\,m^{-3} = 3.73$) with $a = 1.53370(8)$ nm, $b = 0.52991(3)$ nm, $c = 0.84132(4)$ nm, $\beta = 92.278(1)^\circ$ and $V = 0.68321(6)$ nm^3. Final reliability indices are $R_{wp} = 7.32\%$, $R_p = 5.60\%$ and $R_B = 3.22\%$. The powder specimen was also examined by high-temperature XRPD and differential thermal analysis (DTA) to reveal the occurrence of two phase transitions during heating; the space group changed from $P2/c$ to $C2/m$ at ~400 K, followed by the monoclinic-to-hexagonal (or trigonal) transition at 1060 K. The $P2/c$-to-$C2/m$ transition has been, for the first time, described in the yavapaiite-type compounds.

Keywords: Strontium zirconium diorthophosphate; Barium zirconium diorthophosphate; Solid solutions; Phase transitions; Rietveld method

1. Introduction

Double phosphates such as $MZr(PO_4)_2$ with M = Ba, Sr and Ca are promising materials as catalysts, ion exchangers and ion conductors. Their crystal structures and polymorphic sequences have been revealed in previous studies [1–5]. The $BaZr(PO_4)_2$ crystal at ambient temperature is isostructural with yavapaiite ($KFe(SO_4)_2$, space group $C2/m$) [3,6–8]. In the crystal structure, barium is located on $2c$ site and zirconium on $2a$ site, which are coordinated by ten and six oxygen atoms, respectively [3]. The compound $SrZr(PO_4)_2$ undergoes two phase transitions from triclinic to monoclinic, then to hexagonal (or trigonal) during heating [4]. The monoclinic phase is most probably isostructural with yavapaiite as judged by the similarity in X-ray powder diffraction (XRPD) pattern. The structure of $CaZr(PO_4)_2$ is distinct from that of yavapaiite. This compound is orthorhombic with space group $P2_12_12_1$ and free from polymorphic phase transitions [5]. Because both crystals of $SrZr(PO_4)_2$ and $BaZr(PO_4)_2$ belong to a large family of the yavapaiite-related compounds, solid solutions are expected to form over a wide range in the $SrZr(PO_4)_2$–$BaZr(PO_4)_2$ system.

Intracrystalline microstructures in crystals are often induced by phase transitions, which involve changes in space group symmetry. When the low-symmetry (LS) phase is a subgroup of the high-symmetry (HS) phase, two fundamentally different types of microstructures result: antiphase domains (APDs) and twin domains [9]. The APDs arise from the loss of a translational symmetry element whereas the twin domains arise from the loss of a point symmetry element. If the HS and LS phases are of the same point group, the APDs result. This can occur either by the loss of a centering translation (the vector between the origin and a lattice point) and/or by a change in the size of the unit cell. The number of domains (N) produced during the HS-to-LS phase transition can be

*Corresponding author. Fax: +81 52 735 5289.
E-mail address: fukuda.koichiro@nitech.ac.jp (K. Fukuda).

0022-4596/$ - see front matter © 2006 Elsevier Inc. All rights reserved.
doi:10.1016/j.jssc.2006.08.024

predicted by the relationship:

$$N = (\text{change in cell size}) \times (P^{HS} \times L^{HS})/(P^{LS} \times L^{LS}),$$

where P and L represent the point group order and the number of lattice points, respectively [9].

In the present study, a complete series of solid solutions has been successfully prepared in the binary system. We have subsequently determined the crystal structure of the intermediate solid solution from XRPD data using direct methods. The powder specimens were further examined at high temperatures to demonstrate the occurrence of phase transitions.

2. Experimental

2.1. Synthesis

Crystals of $Sr_xBa_{1-x}Zr(PO_4)_2$ with $x = 0$, 0.1, 0.2, 0.3, 0.4, 0.5, 0.6, 0.7, 0.8, 0.9 and 1 were prepared. The stoichiometric mixtures of reagent-grade chemicals $BaCO_3$, $SrCO_3$, m-ZrO_2 and $NH_4H_2PO_4$ were pressed into pellets (12 mm diameter and 3 mm thick), heated at 1673 K for 5 h, followed by quenching in air.

2.2. Characterization

The XRPD patterns for phase identification and for determination of unit-cell parameters were collected at 298 K on a PANalytical X'Pert diffractometer in Bragg–Brentano geometry using monochromatized Cu$K\alpha$ radiation (50 kV, 40 mA) and a step-scan technique in a 2θ range from 10° to 70° with a fixed counting time (t) of 10 s/step and a step interval of 0.02°. The XRPD intensities for structural determination were collected at 298 K in the 2θ range from 10° to 149.98° with $t = 40$ s/step. The divergence slit of 1° was employed, which enabled us to collect the quantitative profile intensity data in the range $2\theta \geqslant 19°$.

The thermal behavior was investigated up to 1473 K by a differential thermal analysis (DTA, Model TG8120, Rigaku Co., Tokyo, Japan). The temperature was controlled by a Pt–PtRh (10%) thermocouple, with heating and cooling rates of 10 K/min. The XRPD patterns at high temperatures for phase identification and refinement of cell parameters were collected on the diffractometer equipped with a heating stage. The profile data with $t = 10$ s/step were collected in the 2θ range from 15° to 70° during stepwise heating up to 1473 K (step width = ~20 K and/or ~100 K). A programmable divergence slit was employed to maintain an illumination length of 10 mm on the sample to realize an illumination area of $10 \times 9\,mm^2$ regardless of the 2θ value. The temperature scale was calibrated up to 1073 K by the measurement of the thermal expansion of Au powder [10].

3. Results and discussion

3.1. Phase constitution and unit-cell parameters of $Sr_xBa_{1-x}Zr(PO_4)_2$

The $Sr_xBa_{1-x}Zr(PO_4)_2$ crystals formed a complete series of solid solutions. The XRPD pattern of $x = 0.1$ was comparable to that of $BaZr(PO_4)_2$ ($x = 0$) [3]. The unit-cell parameters were refined by the Pawley method [11] in the 2θ range from 19° to 37° on a computer program WPPF [12] (Table 1).

For the XRPD patterns with $0.2 \leqslant x \leqslant 0.7$, the peak positions and relative intensities were almost similar to those of $BaZr(PO_4)_2$; however, several weak extra reflections were observed. The relative intensities of these reflections steadily increased with increasing x-value from 0.2 to 0.7. Thus, the peak positions of the crystal with $x = 0.7$ were determined after $K\alpha_2$ stripping on a computer program POWDERX [13], followed by the indexing procedure on a computer program TREOR90 [14]. In the latter procedure, 2θ values of 39 peak positions were used as input data. Only one monoclinic cell was found with satisfactory figures of merit $M_{20}/F_{20} = 18/27(0.008997,84)$, $M_{30}/F_{30} = 16/24(0.007911,0)$ and $M_{39}/F_{39} = 15/25(0.006993,231)$ [15,16]. The derived unit-cell parameters were $a = 1.5323(2)$ nm, $b = 0.52943(4)$ nm, $c = 0.8405(1)$ nm and $\beta = 92.33(1)°$. The unit cell corresponds to a supercell with lattice vectors $2\mathbf{c}_m$, $\mathbf{b}_m$, $\mathbf{a}_m$, where $\mathbf{a}_m$, $\mathbf{b}_m$ and $\mathbf{c}_m$ are the unit-cell vectors of $BaZr(PO_4)_2$ (space group $C2/m$). The unit-cell parameters of the crystals with $0.2 \leqslant x \leqslant 0.6$ were refined by the Pawley method (Table 1). The crystallographic data of $x = 0.7$ were determined by the Rietveld method in the succeeding section.

We defined the normalized unit-cell volume by V/Z, where Z is the number of formula units per unit cell. Because the ionic radii of Sr^{2+} is smaller than that of Ba^{2+}, the replacement of Ba by Sr in the solid solutions with $0 \leqslant x \leqslant 0.7$ steadily decreased the V/Z value (Fig. 1).

The crystals with $x = 0.8$ and 0.9 were composed of both the above-mentioned unknown phase and the triclinic phase, the latter being isostructural with $SrZr(PO_4)_2$ ($x = 1$). This crystal undergoes the monoclinic-to-triclinic phase transition on cooling, which is accompanied by the volumetric contraction of ~6% [4]. Thus, the V/Z value of $SrZr(PO_4)_2$ ($= 0.1557\,nm^3$) was much smaller than those of the solid solutions with $0 \leqslant x \leqslant 0.7$.

3.2. Structure determination of $Sr_{0.7}Ba_{0.3}Zr(PO_4)_2$

For the crystal with $x = 0.7$, the integrated intensities were refined by the Pawley method, and examined to confirm the presence and absence of reflections. There were systematic absence $l \neq 2n$ for $h0l$ reflections, implying that the possible space groups are Pc and $P2/c$. Both the space groups were tested using the EXPO2004 package [17] for crystal-structure determination in the 2θ range of 10.0–149.98°. The lower reliability index R_F [18] of 11.1% was obtained with the latter space group in a

Table 1
Crystal data of $Sr_{0.7}Ba_{0.3}Zr(PO_4)_2$

x	Space group	Z	Unit-cell parameter							Reference
			a (nm)	b (nm)	c (nm)	α/°	β/°	γ/°	V (nm)^3	
0	$C2/m$	2	0.85629(3)	0.53082(2)	0.78956(2)	—	93.086(1)	—	0.35836(2)	[3]
0.1	$C2/m$	2	0.8558(1)	0.53184(6)	0.7877(1)	—	92.96(1)	—	0.3581(1)	Present study[a]
0.2	$P2/c$	4	1.5681(5)	0.53100(4)	0.85282(7)	—	92.788(9)	—	0.7093(1)	Present study[a]
0.3	$P2/c$	4	1.5628(1)	0.53146(5)	0.85216(9)	—	92.64(1)	—	0.7070(1)	Present study[a]
0.4	$P2/c$	4	1.5553(1)	0.53103(6)	0.8492(1)	—	92.53(1)	—	0.7006(1)	Present study[a]
0.5	$P2/c$	4	1.5494(1)	0.52824(5)	0.84370(7)	—	92.48(1)	—	0.6899(1)	Present study[a]
0.6	$P2/c$	4	1.5435(3)	0.52815(5)	0.84100(7)	—	92.272(9)	—	0.6850(1)	Present study[a]
0.7	$P2/c$	4	1.53370(8)	0.52991(3)	0.84132(4)	—	92.278(1)	—	0.68321(6)	Present study[b]
1	$P\bar{1}$	2	0.77508(4)	0.78887(5)	0.51251(3)	95.754(3)	90.228(2)	92.474(2)	0.31149(3)	[4]

Crystals of $0.8 \leqslant x \leqslant 0.9$ are composed of two phases with space groups $P2/c$ and $P\bar{1}$.
[a]Unit-cell parameters refined by Pawley method.
[b]Unit-cell parameters refined by Rietveld method.

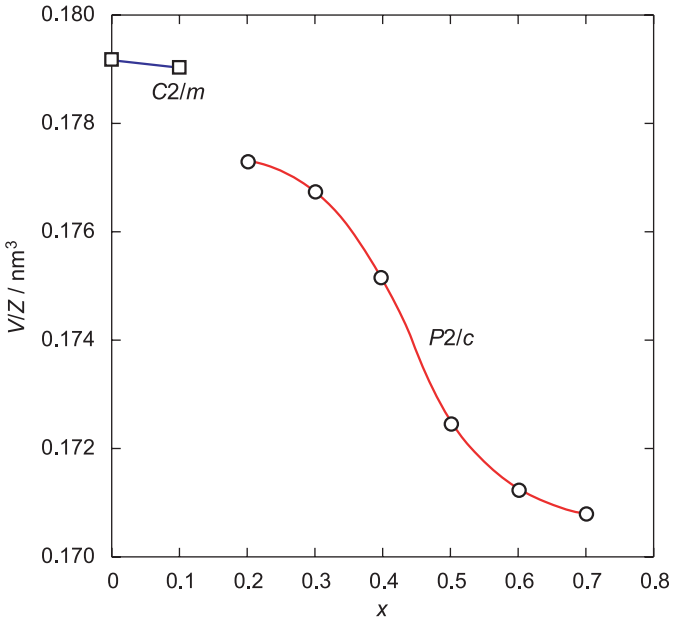

Fig. 1. Normalized unit-cell volume V/Z vs. Sr content (x) for the solid solutions $Sr_xBa_{1-x}Zr(PO_4)_2$ ($0 \leqslant x \leqslant 0.7$), where Z is the number of formula units per unit cell.

default run of the program. Structural parameters of all atoms were refined by the Rietveld method on a computer program RIETAN-2000 [19] using the profile intensity data in the 2θ range of 19.0–149.98° (Fig. 2). The background intensities were fitted to a polynomial function with 12 adjustable parameters. The pseudo-Voigt function [20] was used to fit the peak profile. The preferred orientation parameter of March–Dollase function [21], r, was refined to be $r = 0.868(1)$ with the preferred-orientation vector [100], suggesting that the crystals were fractured along the distinct cleavage planes parallel to (100). All of the isotropic atomic displacement parameters (B) of oxygen atoms were constrained to have the same value. The individual occupancies on M1 and M2 sites were refined under the constraint that the total number of strontium and barium atoms was unchanged. The difference between these occupancies cannot be regarded as significant; thus the site occupancies on both sites were finally fixed to be 30% barium and 70% strontium. Reliability indices for a final result were $R_{wp} = 7.32\%$, $R_p = 5.60\%$ and $R_B = 3.22\%$. [18]. The refined unit-cell parameters are given in Table 1, and final positional and B parameters of atoms are given in Table 2.

3.3. Structure description of $Sr_{0.7}Ba_{0.3}Zr(PO_4)_2$

The crystal-structure models were visualized with a software package VENUS [22]. Fig. 3 shows sections of the crystal structure of $Sr_{0.7}Ba_{0.3}Zr(PO_4)_2$. Selected interatomic distances, together with their standard uncertainties, are listed in Table 3. The mean P1–O and P2–O bond lengths in the PO_4 tetrahedra (respectively, 0.153 and 0.154 nm) are in good agreement with those found in other orthophosphates $Zr_2O(PO_4)_2$ [23], $CaZr(PO_4)_2$ [5], $SrZr(PO_4)_2$ [4] and $BaZr(PO_4)_2$ [3]. The Zr atom is six-fold coordinated with the mean Zr–O distance of 0.207 nm, which is comparable to those of the ZrO_6 octahedra in $CuZr_2(PO_4)_3$ (the mean = 0.207 nm) [24], $CaZr_4(PO_4)_6$ (0.206 nm) [25], $K_2Zr(PO_4)_2$ (0.207 nm) [26] and $BaZr(PO_4)_2$ (0.207 nm) [3]. Ionic radii of P^{5+} in the four-fold coordination [$r(P^{5+}(4)) = 0.017$ nm and $r(O^{2-}(4)) = 0.138$ nm] and Zr^{4+} in the six-fold coordination [$r(Zr^{4+}(6)) = 0.072$ nm and $r(O^{2-}(6)) = 0.140$ nm] predict the interatomic distances of 0.155 nm for P–O and 0.212 nm for Zr–O [27]. These predicted values are in good agreement with the corresponding mean interatomic distances. Bond-valence-sum calculations [28,29] are typical for the species involved: P1 4.83, P2 4.81 and Zr 4.22 (expected values: P 5.00 and Zr 4.00 valence units). The Ba and Sr atoms on M1 and M2 sites are coordinated to ten oxygen atoms (Fig. 3) with nearly the same mean interatomic distances of 0.291 nm for M1 and 0.292 nm for M2 (Table 3). These values are slightly shorter than the

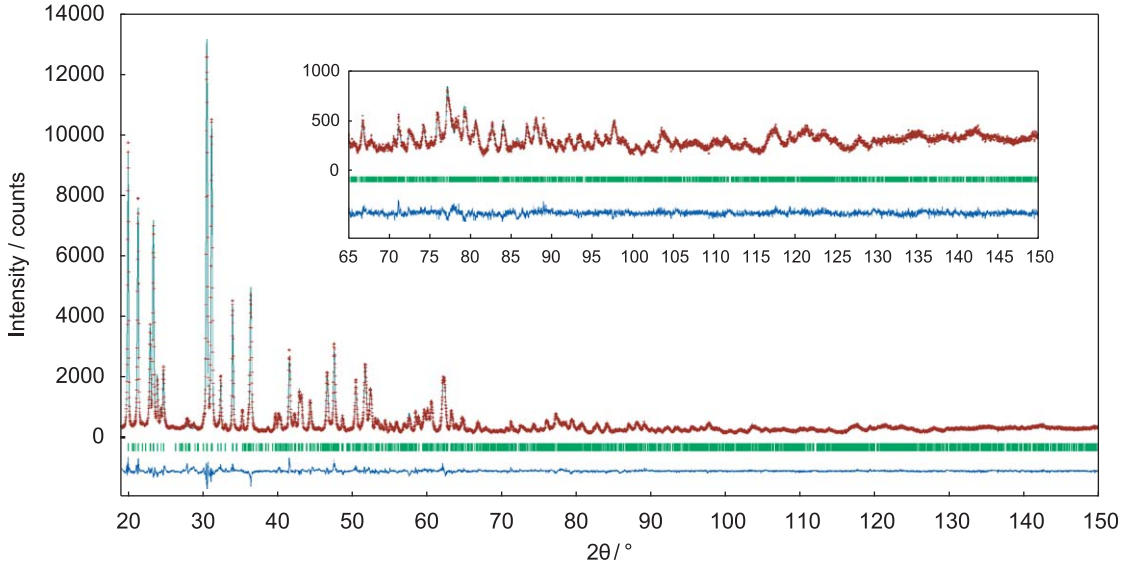

Fig. 2. Comparison between observed (+ marks) and calculated (upper solid line) patterns of $Sr_{0.7}Ba_{0.3}Zr(PO_4)_2$. The difference curve is shown in the lower part of the figure. Vertical marks indicate the positions of possible Bragg reflections.

Table 2
Structural parameters of $Sr_{0.7}Ba_{0.3}Zr(PO_4)_2$

Atom	Site	x	y	Z	B (nm)^2
M1[a]	2*e*	0	0.796(1)	1/4	0.011(1)
M2[a]	2*f*	1/2	0.697(1)	1/4	0.011(1)
Zr	4*g*	0.2499(4)	0.257(1)	0.7547(7)	0.0053(5)
P1	4*g*	0.1400(8)	0.753(2)	0.884(1)	0.011(3)
P2	4*g*	0.3647(7)	0.231(2)	0.115(1)	0.009(3)
O1	4*g*	0.150(1)	0.508(2)	0.789(2)	0.005(1)
O2	4*g*	0.0540(7)	0.755(4)	0.971(1)	0.005
O3	4*g*	0.149(1)	0.986(2)	0.779(2)	0.005
O4	4*g*	0.2139(8)	0.738(5)	0.012(1)	0.005
O5	4*g*	0.3011(9)	0.242(5)	−0.030(1)	0.005
O6	4*g*	0.334(1)	0.567(2)	0.732(2)	0.005
O7	4*g*	0.355(1)	0.026(2)	0.697(2)	0.005
O8	4*g*	0.4584(7)	0.269(5)	0.062(1)	0.005

[a]Sr/(Ba + Sr) = 0.7.

mean Ba–O distance (0.296 nm) of $BaZr(PO_4)_2$, in which the Ba atoms are ten-fold coordinated.

The crystal structure of $Sr_{0.7}Ba_{0.3}Zr(PO_4)_2$ consists of the five types of polyhedra, $M1O_{10}$, $M2O_{10}$, ZrO_6, $P1O_4$ and $P2O_4$. The $M1O_{10}$ polyhedra share the O2–O2 edges to form a continuous sheet (denoted by A) with the general formula $(M1O_6)^{10-}$ (Fig. 3(c)). The $M2O_{10}$ polyhedra also form a sheet (B) with the formula $(M2O_6)^{10-}$ by sharing the O8–O8 edges (Fig. 3(a)). The ZrO_6, $P1O_4$ and $P2O_4$ polyhedra share the apices to form the sheet (C) parallel to (100) (Fig. 3(b)). These sheets are stacked in the [100] direction with an ACBC repeat within the unit cell, and they are linked through the oxygen atoms to form a three-dimensional structure (Fig. 4). Since the atom arrangement is similar to that of $BaZr(PO_4)_2$, the crystal may be grouped into a large family of the yavapaiite-related compounds.

3.4. Phase transitions of $Sr_{0.7}Ba_{0.3}Zr(PO_4)_2$

The high-temperature XRPD showed that, during the heating process up to 393 K (step width = ~20 K), the intensities of superstructure reflections 110, 310, $\bar{1}12$ and 112 gradually decreased. At temperatures 413–973 K, all the reflections were successfully indexed on the monoclinic basic cell (Fig. 5). The peak positions and their relative intensities were very similar to those of $BaZr(PO_4)_2$ [3]. This implies that the high-temperature phase is most probably isostructural with yavapaiite (space group $C2/m$). The cell parameters at 448 K were refined by the Pawley method to be $a_m = 0.84352(8)$ nm, $b_m = 0.53038(5)$ nm, $c_m = 0.76651(7)$ nm, $\beta_m = 92.285(4)^\circ$ and $V_m = 0.34265(6)$ nm^3. The $P2/c$-to-$C2/m$ transition, which occurred at ~400 K with $x = 0.7$, has been for the first time described in the yavapaiite-type compounds.

The polyhedral parameters of $Sr_{0.7}Ba_{0.3}Zr(PO_4)_2$ at 298 K were found from calculation using a computer program IVTON [30] (Table 4). The polyhedral parameters of the high-temperature phase at 448 K were determined from calculations based on the cell parameters aforementioned and structural parameters of $BaZ(PO_4)_2$ [3]. In the hypothetical crystal structure, the Ba and Sr atoms are statistically distributed over the ten-coordination site (denoted by Me site). The MeO_{10} polyhedra in the high-temperature phase become the $M1O_{10}$ and $M2O_{10}$ polyhedra in the low-temperature phase. The comparison of distortion parameters (Δ and σ) between the corresponding polyhedra shows that the $C2/m$-to-$P2/c$ transition is accompanied by the relatively large deformation of MeO_{10} and ZrO_6 polyhedra; the maximum amount of deformation occurs with the polyhedral change from MeO_{10} to $M1O_{10}$. This change is also accompanied by a

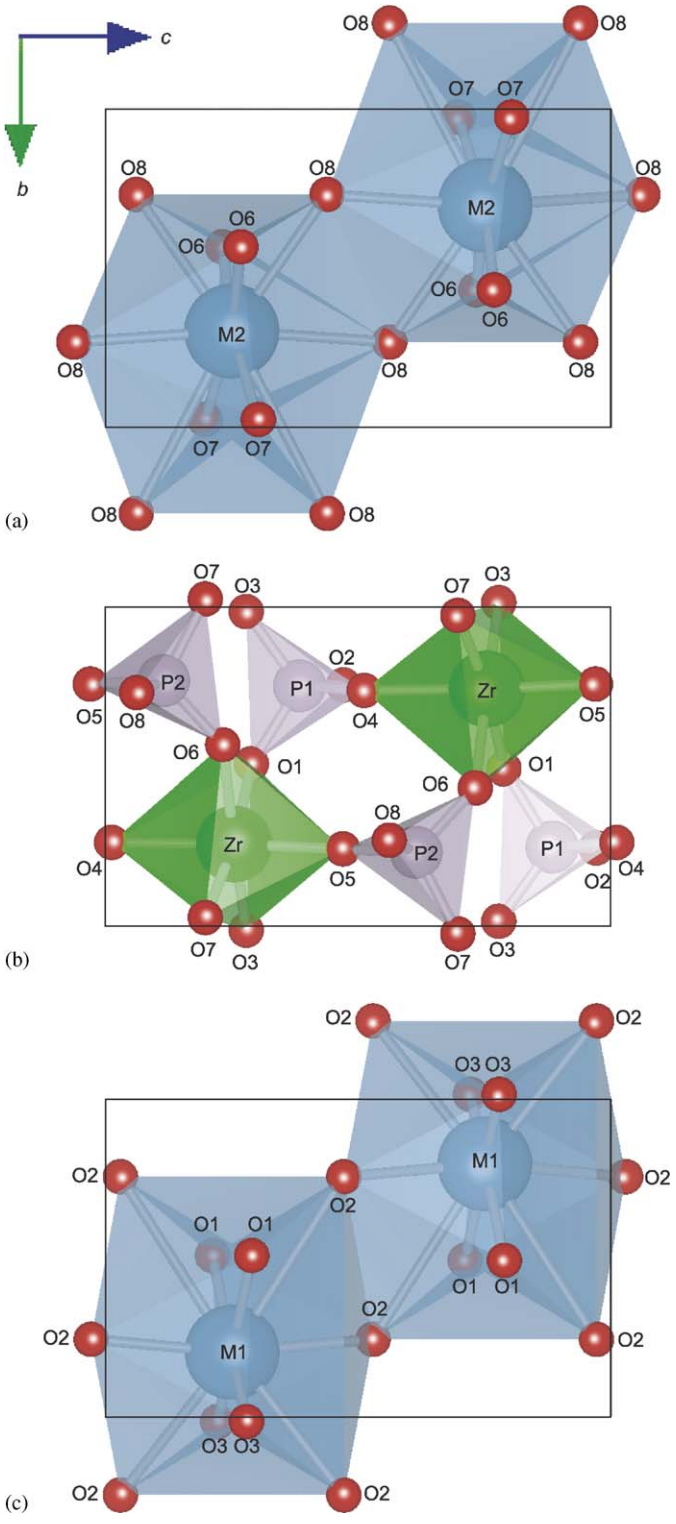

Fig. 3. Parts of the $Sr_{0.7}Ba_{0.3}Zr(PO_4)_2$ structure viewed along the *a*-axis. Atom numbering corresponds to that given in Table 2. Linkage patterns of (a) $M2O_{10}$ polyhedra at $x\sim0.5$, (b) ZrO_6, $P1O_4$ and $P2O_4$ polyhedra at $x\sim0.25$ and (c) $M1O_{10}$ polyhedra at $x\sim0$. The unit cell depicted by open squares.

large volumetric expansion of 4.0%, whereas the largest expansion of 4.5% occurs with the ZrO_6 polyhedra. Neither the deformation nor volumetric change was recognized for the PO_4 tetrahedra during the transition. Accordingly, the $C2/m$-to-$P2/c$ transition would be principally caused by the orientational disorder of PO_4 tetrahedra.

The space group change from $C2/m$ to its subgroup $P2/c$ is accompanied by a loss of the centering translation as well as an increase in the size of the unit cell, while the point group symmetry is retained. The point group $2/m$ of both high- and low-temperature phases has four point symmetry elements. The *C*-centered lattice of the high-temperature phase has two lattice points per unit cell, and the primitive lattice of the low-temperature phase has one lattice point per unit cell. The size of the unit cell is increased by 2 during the transition. Because the translation vectors (i.e., 1/2[110], [001] and 1/2[112] of the high-temperature phase) are lost during the transition, we expect the formation of APDs; the number of variants possible to produce during the phase transition is 4 $[=2\times(4\times2)/(4\times1)]$ [9]. The four variants are related across the antiphase boundaries by the displacement vectors 1/2[011], 1/2[100] and 1/2[211] of the low-temperature phase. The displacement vectors in the high-temperature phase can acquire different energies in the low-temperature phase. Thus this energy difference can favor the formation of one orientation over the other.

For the profile intensity data taken above 1073 K, all the reflections were successfully indexed on a hexagonal unit cell (Fig. 5). The refined cell parameters at 1473 K are $a_h = 0.51657(3)$ nm, $c_h = 0.77382(5)$ nm and $V_h = 0.17882(3)$ nm^3 with the possible crystal system being hexagonal or trigonal. Thus, the endothermic effect of DTA at 1060 K during heating was assigned as the phase transition from monoclinic (space group $C2/m$) to hexagonal (or trigonal). Upon cooling, the exothermic effect of DTA at 934 K would be due to the reverse phase transition. The probable lattice correspondence between the two polymorphs is

$$\begin{bmatrix}\mathbf{a}_h\\ \mathbf{b}_h\\ \mathbf{c}_h\end{bmatrix} = \begin{bmatrix}1 & \bar{1} & 0\\ 1 & 0 & 0\\ 0 & 0 & 1\end{bmatrix}\begin{bmatrix}\mathbf{a}_m\\ \mathbf{b}_m\\ \mathbf{c}_m\end{bmatrix},$$

where $\mathbf{a}_m$, $\mathbf{b}_m$ and $\mathbf{c}_m$ are the unit-cell vectors of the monoclinic phase and $\mathbf{a}_h$, $\mathbf{b}_h$ and $\mathbf{c}_h$ are those of the hexagonal phase. The transformation between the two phases would be of the displacive type.

4. Conclusion

A complete series of solid solutions was prepared in the $SrZr(PO_4)_2$–$BaZr(PO_4)_2$ binary system. We determined the crystal structure of $Sr_{0.7}Ba_{0.3}Zr(PO_4)_2$ at 298 K, being monoclinic with space group $P2/c$. The structure consists of the five types of polyhedra, $M1O_{10}$, $M2O_{10}$, ZrO_6, $P1O_4$ and $P2O_4$. The Ba and Sr atoms are equally distributed

Table 3
Selected interatomic distances (nm) and angles (°) of $Sr_{0.7}Ba_{0.3}Zr(PO_4)_2$

M1–O1[a]	0.282(1)	M2–O6[g]	0.290(2)	Zr–O[l]	0.206(2)	P1–O1	0.154(2)	P2–O5[c]	0.153(1)
M1–O1[b]	0.282(1)	M2–O6[b]	0.290(2)	Zr–O3[m]	0.213(2)	P1–O2	0.153(2)	P2–O6[b]	0.154(2)
M1–O2[c]	0.2529(9)	M2–O7[g]	0.269(1)	Zr–O4[l]	0.209(1)	P1–O3	0.153(2)	P2–O7[o]	0.154(2)
M1–O2[d]	0.2529(9)	M2–O7[b]	0.269(1)	Zr–O5	0.195(1)	P1–O4[n]	0.153(9)	P2–O8	0.154(2)
M1–O2[a]	0.354(2)	M2–O8	0.282(2)	Zr–O6	0.210(1)	O1–P1–O2	111.1(10)	O5[c]–P2–O6[b]	106.3(10)
M1–O2[e]	0.311(2)	M2–O8[h]	0.347(2)	Zr–O7	0.210(2)	O1–P1–O3	111.7(10)	O5[c]–P2–O7[o]	108.7(11)
M1–O2[b]	0.354(2)	M2–O8[i]	0.282(2)			O1–P1–O4[n]	103.6(11)	O5[c]–P2–O8	109.7(11)
M1–O2[f]	0.311(2)	M2–O8[j]	0.347(2)			O2–P1–O3	111.7(10)	O6[b]–P2–O7[o]	106.9(10)
M1–O3[e]	0.256(2)	M2–O8[k]	0.2732(9)			O2–P1–O4[n]	106.9(11)	O6[b]–P2–O8	114.19(10)
M1–O3[f]	0.256(2)	M2–O8[l]	0.2732(9)			O3–P1–O4[n]	111.5(11)	O7[o]–P2–O8	110.8(10)

Symmetry transformations used to generate equivalent atoms: a: $-x$, $1-y$, $1-z$; b: x, $1-y$, $-1/2+z$; c: x, y, $-1+z$; d: $-x$, y, $3/2-z$; e: $-x$, $2-y$, $1-z$; f: x, $2-y$, $-1/2+z$; g: $1-x$, $1-y$, $1-z$; h: x, $1+y$, z; i: $1-x$, y, $1/2-z$; j: $1-x$, $1+y$, $1/2-z$; k: $1-x$, $1-y$, $-z$; l: x, $1-y$, $1/2+z$; m: x, $-1+y$, z; n: x, y, $1+z$; o: x, $-y$, $-1/2+z$.

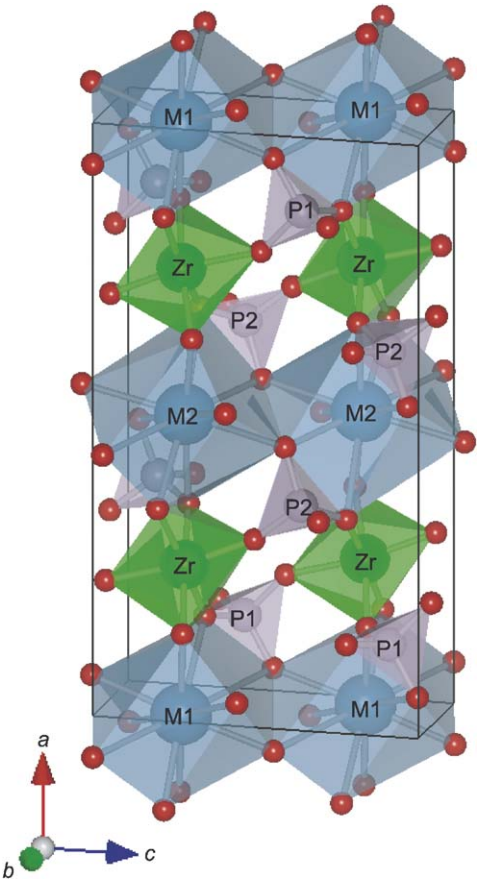

Fig. 4. Crystal structure of $Sr_{0.7}Ba_{0.3}Zr(PO_4)_2$.

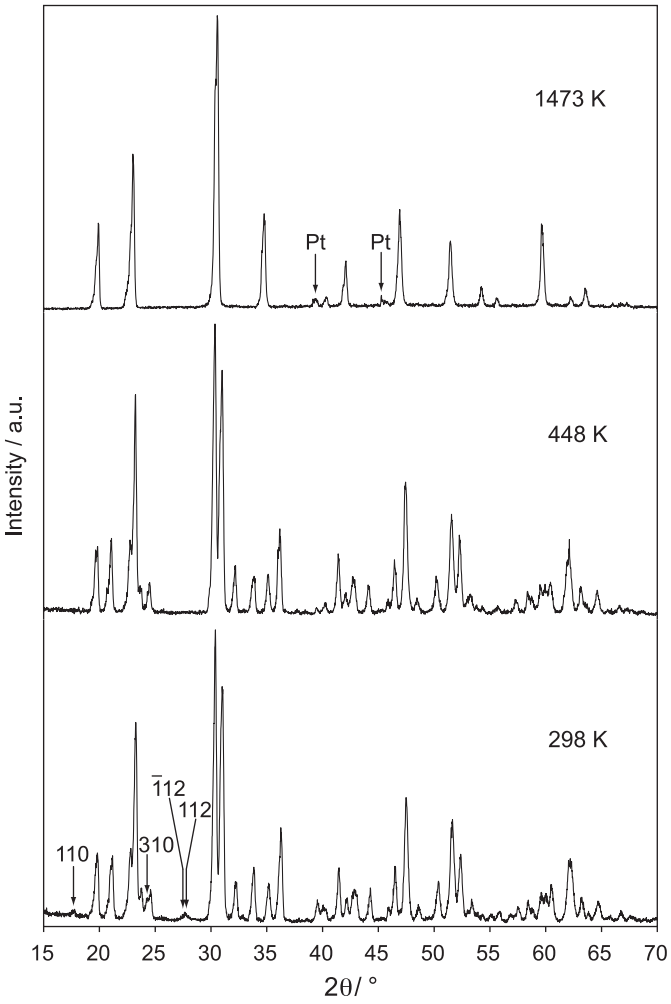

Fig. 5. Changes in powder XRPD pattern induced by two phase transitions from monoclinic (space group $P2/c$) to monoclinic ($C2/m$), then to hexagonal (or trigonal) during heating from 298 to 1473 K. Arrows in the lower XRPD pattern indicate the positions of superstructure reflections. Arrows in the upper XRPD pattern indicate the positions of 111 and 200 reflections with the platinum heating filament.

over M1 and M2 sites. The $M1O_{10}$ polyhedra share the edges to form a two-dimensional sheet parallel to (100). The $M2O_{10}$ polyhedra also form a sheet by sharing edges. The ZrO_6, $P1O_4$ and $P2O_4$ polyhedra share the apices to form a sheet parallel to (100). These sheets are stacked in the [100] direction, and they are linked through the oxygen atoms to form a three-dimensional structure. Upon heating, the space group changed from $P2/c$ to $C2/m$ at ~400 K, followed by the monoclinic-to-hexagonal (or trigonal) transition at 1060 K. The former phase transition was accompanied by the disappearance of superstructure along the a-axis. The $P2/c$–to-$C2/m$ transition has been, for the first time, described in the yavapaiite-type compounds.

Table 4
Polyhedral parameters of $Sr_{0.7}Ba_{0.3}Zr(PO_4)_2$ at 298 and 448 K

Polyhedron	Δ (nm)	r_s (nm)	σ	V_P (nm)^3
298 K (space group P2/c)				
$M1O_{10}$	0.272	0.291	0.875	0.0496
$M2O_{10}$	0.267	0.292	0.911	0.0475
ZrO_6	0.075	0.207	0.979	0.0116
$P1O_4$	0.005	0.153	1	0.0018
$P2O_4$	0.005	0.154	1	0.0019
448 K (space group C2/m)				
MeO_{10}	0.000	0.292	0.933	0.0477
ZrO_6	0.000	0.203	0.998	0.0111
PO_4	0.005	0.152	1	0.0018

Δ = eccentricity; r_s = radius of sphere fitted to ligands; σ = sphericity; V_P = volume of coordination polyhedron; σ for coordination number four is 1 by definition.

References

[1] K. Popa, R.J.M. Konings, P. Boulet, D. Bouexiere, A.F. Popa, Thermochim. Acta 436 (2005) 51–55.
[2] T. Geisler, K. Popa, R.J.M. Konings, A.F. Popa, J. Solid State Chem. 179 (2006) 1490–1496.
[3] K. Fukuda, A. Moriyama, T. Iwata, J. Solid State Chem. 178 (2005) 2144–2151.
[4] K. Fukuda, A. Moriyama, S. Hashimoto, J. Solid State Chem. 177 (2004) 3514–3521.
[5] K. Fukuda, K. Fukutani, Powder Diffract. 18 (2003) 296–300.
[6] E.J. Graeber, A. Rosenzweig, Am. Miner. 56 (1971) 1917–1933.
[7] M. Th. Paques-Ledent, J. Inorg. Nucl. Chem. 39 (1977) 11–17.
[8] R. Masse, A. Durif, C. R. Seances Acad. Sci. Ser. C 274 (1972) 1692–1695.
[9] G.L. Nord Jr., In: P.R. Buseck (Ed.), Minerals and Reactions at the Atomic Scale: Transmission Electron Microscopy: Imaging Transformation-Induced Microstructures, Mineralogical Society of America, Washington, DC, USA, 1992, pp. 455–508.
[10] R.O. Simmons, J. Appl. Phys. 41 (1970) 2235–2240.
[11] G.S. Pawley, J. Appl. Crystallogr. 14 (1981) 357–361.
[12] H. Toraya, J. Appl. Crystallogr. 19 (1986) 440–447.
[13] C. Dong, J. Appl. Crystallogr. 32 (1999) 838.
[14] P.E. Werner, L. Eriksson, M. Westdahl, J. Appl. Crystallogr. 18 (1985) 367–370.
[15] P.M. de Wolff, J. Appl. Crystallogr. 1 (1968) 108–113.
[16] G.S. Smith, R.L. Snyder, J. Appl. Crystallogr. 12 (1979) 60–65.
[17] A. Altomare, M.C. Burla, M. Camalli, B. Carrozzini, G.L. Cascarano, C. Giacovazzo, A. Guagliardi, A.G.G. Moliterni, G. Polidori, R. Rizzi, J. Appl. Crystallogr. 32 (1999) 339–340.
[18] R.A. Young, in: R.A. Young (Ed.), The Rietveld Method, Oxford University Press, Oxford, UK, 1993, pp. 1–38.
[19] F. Izumi, T. Ikeda, Mater. Sci. Forum 321–324 (2000) 198–203.
[20] H. Toraya, J. Appl. Crystallogr. 23 (1990) 485–491.
[21] W.A. Dollase, J. Appl. Crystallogr. 19 (1986) 267–272.
[22] F. Izumi, R. A. Dilanian, in: Recent Research Developments in Physics, vol. 3, Part II, Transworld Research Network, Trivandrum, India, 2002, pp. 699–726.
[23] W. Gebert, E. Tillmanns, Acta Crystallogr. B 31 (1975) 1768–1770.
[24] I. Bussereau, M.S. Belkhiria, P. Gravereau, A. Boireau, J.L. Soubeyroux, R. Olazcuaga, G. Le Flem, Acta Crystallogr. C 48 (1992) 1741–1744.
[25] J. Alamo, J.L. Rodrigo, J. Solid State Chem. 63–65 (1993) 678–683.
[26] M. Dorffel, J. Liebertz, Zeit. Kristallogr. 193 (1990) 155–159.
[27] R.D. Shannon, Acta Crystallogr. A 32 (1976) 751–767.
[28] I.D. Brown, D. Altermatt, Acta Crystallogr. B 41 (1985) 244–247.
[29] N.E. Brese, M. O'Keeffe, Acta Crystallogr. B 47 (1991) 192–197.
[30] T. Balic-Zunic, I. Vickovic, Acta Crystallogr. 29 (1996) 305–306.